Directed evolution of a bright variant of mCherry: Suppression of non-radiative decay by fluorescence lifetime selections

Srijit Mukherjee* [1, 2], Premashis Manna* [3], Sheng-Ting Hung [4], Felix Vietmeyer [1], Pia Friis [1], Amy E. Palmer [5, 6], and Ralph Jimenez [1, 2]

[1] *JILA, University of Colorado, Boulder and National Institute of Standards and Technology, 440 UCB,* Boulder, Colorado 80309, United States

[2] Department of Chemistry, University of Colorado, Boulder, 215 UCB, Boulder, Colorado 80309, United States

[3] Department of Chemistry, Massachusetts Institute of Technology, Cambridge, Massachusetts 02139, United States

[4] Department of Physics, National Sun Yat-sen University, Kaohsiung 80424, Taiwan

[5] Department of Biochemistry, University of Colorado at Boulder, 596 UCB, Boulder, Colorado 80309, United States

[6] BioFrontiers Institute, University of Colorado, Boulder, 596 UCB, Boulder, Colorado 80309, United States

* Equal contributions

Abstract

The approximately linear scaling of fluorescence quantum yield (ϕ) with fluorescence lifetime (τ) in fluorescent proteins (FPs) has inspired engineering of brighter fluorophores based on screening for increased lifetimes. Several recently developed FPs such as mTurquoise2, mScarlet and FusionRed-MQV which have become useful for live cell imaging are products of lifetime selection strategies. However, the underlying photophysical basis of the improved brightness has not been scrutinized. In this study, we focused on understanding the outcome of lifetime-based directed evolution of mCherry, which is a popular red-FP (RFP). We identified four positions (W143, I161, Q163, and I197) near the FP chromophore that can be mutated to create mCherry-XL (e**X**tended **L**ifetime: ϕ = 0.70; τ =3.9 ns). The threefold higher quantum yield of mCherry-XL is on par with that of the brightest RFP to date, mScarlet. We examined selected variants within the evolution trajectory and found a near-linear scaling of lifetime with quantum yield and consistent blue-shifts of the absorption and emission spectra. We find that the improvement in brightness is primarily due to a decrease in the non-radiative decay of the excited state. In addition, our analysis revealed the decrease in non-radiative rate is not limited to the blue-shift of the energy gap and changes in the excited state reorganization energy. Our findings suggest that non-radiative mechanisms beyond the scope of energy-gap models such the Englman-Jortner are suppressed in this lifetime evolution trajectory.

Introduction

Fluorescence lifetime-based selections on fluorescent protein (FP) libraries, performed on cell-screening platforms such as microscopes or flow cytometers, have been key to the development of the brightest genetically-encoded fluorophores. [1-3] For example, brighter variants of the red FP (RFP) FusionRed have been generated with microfluidic cell-sorting. [4, 5] The brightest RFP and cyan-FP (CFP) to-date, mScarlet (ϕ = 0.70; τ = 3.9 ns) and mTurquoise2 (ϕ = 0.93; τ = 4.0 ns), respectively were also developed using lifetime selections on imaging platforms. [6, 7] Although these lifetime selections have been unquestionably successful in generating brighter FPs for imaging applications, the intermediates along the evolutionary trajectory generated by these efforts have generally been set aside in favor of focusing on the final product of molecular evolution. Although it is widely acknowledged that lifetime and other photophysical properties such as photobleaching or spectral changes frequently co-evolve, a mechanistic investigation of their interdependence has rarely been pursued. [8]

In the GFP superfamily, the chromophore is formed when a tripeptide of the internal α-helix embedded in an 11-stranded β-barrel undergoes rearrangement, cyclization, dehydration, and oxidation. [9, 10] This process results in a π-conjugated structure of p-hydroxybenzylidine and imidazolinone rings bridged through a methine carbon. In RFPs, the chromophore conjugation is further extended by a N-acylimine moiety that leads to a red-shift of the absorption and emission spectra. [11, 12] A combination of electrostatic and steric interactions from surrounding amino acids tune the ground (S_0) and the excited (S_1) state potential energy surfaces of the chromophore, thus influencing the pathways of excited state depopulation. [13-18] As a result, the unique chromophore environment within each FP determines its fluorescence lifetime. Each functional (i.e., properly-folded and chromophore-matured) FP generated by an engineering effort provides an opportunity to examine a point within the evolutionary trajectory of fluorescence lifetime and other photophysical properties. These properties may be correlated with a particular pathway across the mutational landscape. [19] The global photophysical assessment of an evolutionary trajectory therefore contains vital information that can inform strategies for FP evolution. This is particularly relevant for developing a new FP tailored to a specific application modality- whether it is fluorescence lifetime imaging (FLIM), Forster Resonance Energy Transfer (FRET), or multicolor widefield imaging. [20]

Many theoretical and spectroscopic studies provide an emerging framework for understanding the factors influencing molecular brightness of FPs. [13-18] However, understanding the reasons for interdependence of photophysical properties is a major challenge. Observables such as fluorescence lifetime that directly report on excited state depopulation timescales are sometimes found to be correlated with other photophysical properties that are less directly related to these dynamics. For instance, in an attempt to find a bright, far-red emitting FP, Canty *et al.* generated and sorted mutant libraries in bacteria by gene shuffling mScarlet, which has a long fluorescence lifetime, with mCardinal, which has far-red emission (659 nm). Though the investigators did not meet their original goal, their analysis revealed that fluorescence lifetime and peak emission wavelength are inversely correlated. [21] We employed high-throughput microfluidic screening on mOrange2, TagRFP-T and mCherry and found a similar inverse correlation of fluorescence lifetime and emission wavelength. [1] Moreover, an inverse correlation of fluorescence lifetime and photostability under constant irradiation also suggested that increase in fluorescence lifetime leads to molecules bleaching faster, likely due to the higher reductive potential of the S_1 state. This study also showed that the correlation changed with increasing irradiance, suggesting that mechanisms other than photodegradation from the S_1 state may be at play. An inverse correlation of the fluorescence lifetime and photostability was also reported

in our previous study of FusionRed variants. [5] Further investigations are necessary for gleaning mechanistic insights from these observations.

Spectroscopic, computational, and crystallographic evidence suggest that chromophore planarity and protein rigidity are the primary characteristics of bright FPs. [22-24] Other investigators have considered more subtle physical factors that influence brightness. [15-17] Using physical models such as the Marcus-Hush theory, these studies focused on quantifying and understanding the role of the driving force in charge transfer between the two resonance forms of the GFP chromophore in the ground and excited electronic states.[15] This driving force is vulnerable to electrostatic control from the environment, which regulates access to non-radiative pathways of excited state depopulation, and therefore directly influences brightness. Analogous studies of the RFP chromophore have not yet been reported. Park and Rhee utilized hybrid QM-MM approaches to demonstrate the influence of electrostatic effects on controlling the non-radiative rate of GFP. [13] Their analysis revealed that electric fields control access to photoisomerization channels which dictate ultrafast non-radiative decay. [13] For RFPs, Drobizhev and co-workers demonstrated that the electric field pointing from the oxygen atom on the imidazolinone ring to the oxygen atom on the phenol ring in the chromophore controls access to twisted-intermolecular charge-transfer (TICT) states which promote ultrafast non-radiative relaxation. [14] In summary, the control of non-radiative decay pathways is a major bottleneck in "brightening" FPs.

Despite its poor brightness, mCherry is a popular RFP for cellular sensing and imaging because of its widespread availability in a plethora of fusion constructs. [25, 26] This monomeric RFP traces its lineage from the naturally occurring tetramer DsRed. [27] The consequent engineering strategies on DsRed resulted in a FP with high expression and fast chromophore maturation, low phototoxicity, and a favorable red-shift of absorption and emission spectra. However, mCherry is much dimmer than its progenitor, primarily due to a three-fold drop in fluorescence quantum yield. Previous attempts to develop brighter and red-shifted versions of mCherry have been unable to restore its fluorescence quantum yield to that of DsRed. [22, 24, 28, 29] In this study, we present a monomeric variant denoted mCherry-XL (e**X**tended **L**ifetime: W143S, I161V, Q163Y and I197R) which is 3-fold brighter than mCherry, and matches the molecular brightness of DsRed. We provide insight into the evolution from mCherry ($\phi = 0.22$; $\tau = 1.6$ ns) to mCherry-XL ($\phi = 0.70$; $\tau = 3.9$ ns). We analyzed functional RFPs with the longest lifetimes at two intermediate steps in the evolution trajectory to assess co-evolution of other photophysical properties such as absorption and emission wavelengths. As expected, we observe a near-linear response of increasing quantum yield with lifetime, along with blue shifts in the absorption and emission maxima. Although the analysis of radiative rates reveals small but significant changes, it is primarily the 6.5-fold reduction in the non-radiative rate that leads to the major increase in fluorescence lifetime. Furthermore, our analysis reveals the reductions in non-radiative rate are not entirely due to the changes in the excited state reorganization energy or blue shifting of the absorption and emission profiles. Our lifetime evolution trajectory agrees with the mechanistic proposals of Drobizhev *et al.* and Lin *et. al*, who emphasize electrostatic and steric control of the chromophore, to minimize non-radiative processes beyond the scope of energy-gap-type models. [14, 15]

Methods and materials

a. Mutagenesis, cell growth and sorting

Supplementary Information Section 1, 2 and 3 describes our protocols for cell growth, sample preparation and sorting. Yeast cells (*Saccharomyces cerevisiae* BY4741) transformed with the pYestDest52 vector

containing FPs were used for lifetime-based screening with a microfluidic sorting system developed in our laboratory. [1, 2, 4]

b. Protein purification, *in vitro* measurements

Protocols for *in vitro* measurements have been published earlier. [5] In short, DNA of selected FP variants from yeast were cloned into the bacterial p-Bad-His vector and protein was extracted using Ni-NTA-based column chromatography. Steady state data for spectra, quantum yield and extinction coefficient measurements were collected using a Cary 5000 UV−vis near-IR spectrophotometer in the double beam mode for absorption, and a HORIBA Jobin Yvon Fluorolog-3 FL3-222 instrument for fluorescence and excitation spectra. Fluorescence lifetime and anisotropy decay measurements were collected using a commercial time-correlated single photon counting (TCSPC) system (Fluoro-time 100, PicoQuant) with a 560 nm pulsed laser diode head excitation source and a repetition rate of 5 MHz using a spectral filter centered at 600 nm (60 nm FWHM). The methods used in this measurement have been discussed in reference 5 and the details of the fit and the instrument response function have been provided in the Supplementary Information Section 5. [5] Samples were diluted using 1X-Tris-HCl Buffer (pH ~ 7.4), and measurements were carried out at optical densities (ODs) between 0.05 and 0.25 to ensure measurements fall within the linear regime of the instrument response.

Results

a. A 2.5-fold increase in lifetime is achieved using directed evolution strategies on mCherry.

We utilized lifetime-based microfluidic cell sorting to direct the evolution of mCherry in *S. cerevisiae* (Figure 1) to longer lifetime. First, we created mutagenesis libraries targeting residue numbers 16, 17, 70, 99, and 197 (numbered with respect to mCherry PDB:2H5Q). The variant C12 (mCherry I197R) was identified from the first round of selection. Next, a site-directed library on variant C12 targeting positions 143, 161 and 163 (C12-X library) resulted in clones with lifetime ranging from 1 ns to 4 ns (Figure 1b). A portion of this library was grown on plates and 20 bright variants were selected on lifetime. One of these variants, C12-3 (mCherry W143I, I161C, Q163L and I197R) was selected for further investigation. The C12-X library was then subjected to error-prone mutagenesis followed by another round of lifetime sorting with the sorting gate placed at 3.7 ns (Figure 1b). Selection of variants after this round of lifetime enrichment identified the mutant “SLT-11” (mCherry N98S, R125H, F129L, Q137L, W143S, I161V, Q163Y, and I197R) with τ=3.9 ns. Unfortunately, the SLT-11 variant had poor protein yield in bacteria compared to yeast cells. Therefore, mutations distant from the chromophore (>15 Å) were reverted to those of mCherry (S98N, H125R/K, L129F and L137Q) to boost bacterial expression without compromising the long-lifetime of SLT-11 (Supplementary Figure S3). This process led to the generation of the quadruple mutant "mCherry-XL" (mCherry W143S, I161V, Q163Y, I197R), which was further characterized. Details of library generation and protocols for mutagenesis have been provided in the Supplementary Information (Section 1 and 2). The four FPs (mCherry, C12, C12-3 and mCherry-XL) were characterized *in vitro* and *in cellulo* (Supplementary Information Sections 4 and 5). It was found that mCherry-XL has a 3-fold higher molecular brightness and is 1.5-fold brighter in HeLa cells compared to its progenitor mCherry (Supplementary Figure S5).

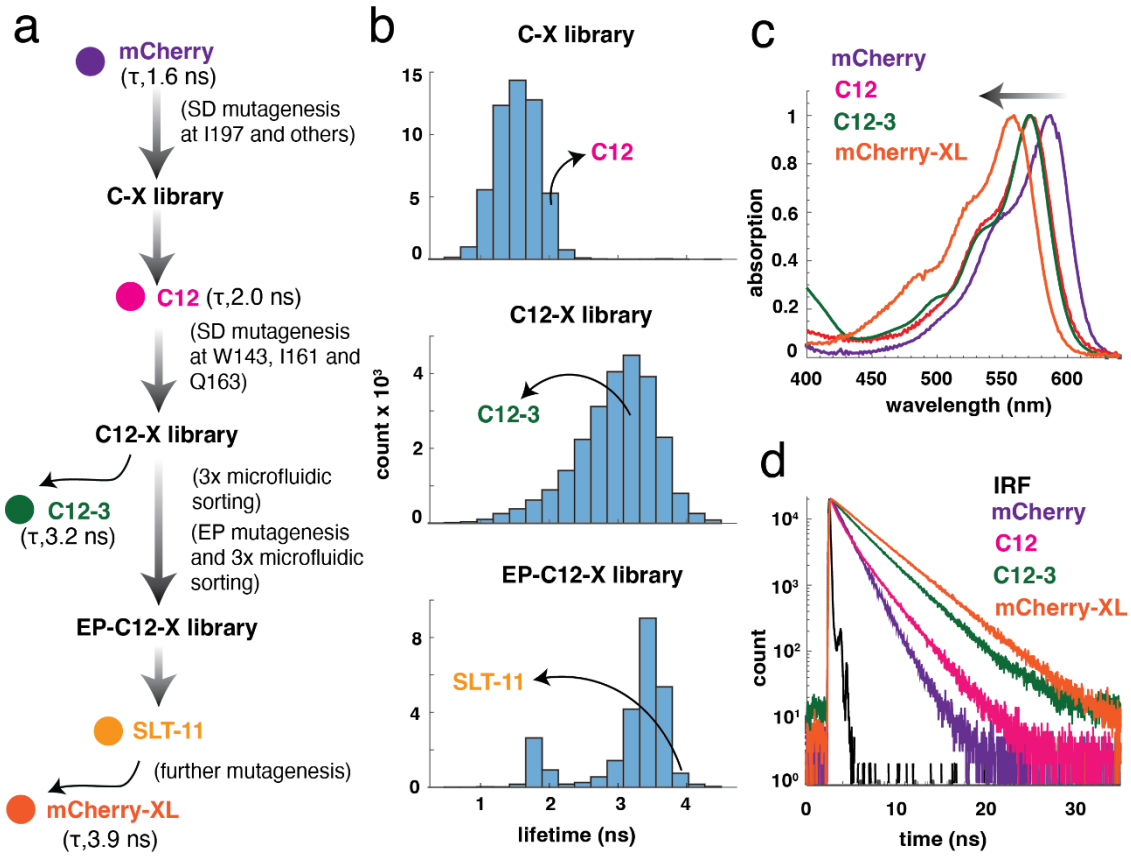

Figure 1: Directed evolution of mCherry resulted in variants with blue-shifts and increased lifetime. (a) The lifetime evolution trajectory from mCherry (τ_{av} =1.6 ns) to mCherry-XL (τ_{av} = 3.9 ns), with intermediate clones (shown in filled circles) selected for photophysical analysis (barring the exception of SLT-11). SD and EP mutagenesis refer to site-directed and error-prone mutagenesis respectively. (b) Lifetime histograms of mCherry libraries at the different stages of evolution. The lifetime histograms characterize libraries expressed in yeast cells screened on a microfluidic platform developed in our laboratory. [1, 2, 4, 5] The number of cells screened in each panel were 52382, 24998 and 25617 for C-X, C12-X and EP-C12-X library respectively. (c & d) Absorption and fluorescence lifetime decays of the variants. The arrow in c indicates blue-shift in the absorption of the variants compared to their precursor mCherry.

b. Improved brightness is primarily achieved by suppressing the rate of non-radiative relaxation.

We performed *in vitro* photophysical measurements on mCherry, C12, C12-3, and mCherry-XL (Table 1). Fluorescence lifetime decays were fit to the appropriate exponential decay functions (Supplementary Figure S10). Except for C12, a shift from multi-exponential to a mono-exponential decay is observed in this series, where the amplitude and the time constant of the major decay component both increase. The timescale of the shorter component (~1 ns) is approximately the same for all four variants (Table 2). Fluorescence anisotropy measurements on these FPs revealed rotational diffusion constants similar to those of monomeric proteins like mCherry, indicating that the mutations did not lead to dimerization or higher order oligomerization (Supplementary Figure S9).

Table 1: Spectral and photophysical properties of the mCherry variants. Error bars indicate standard deviations from triplicate measurements. Details of the experimental methods have been presented in SI Section 5.

Variant	λ_{abs} (nm)	E_{abs} (cm^{-1})	λ_{em} (nm)	E_{em} (cm^{-1})	Stokes shift (cm^{-1})	ϕ (%)	Lifetime (ns)	ε_{max} ($M^{-1}cm^{-1}$)
mCherry	587	17036	609	16420	615	22 (ref)	1.65 ± 0.07	76000 ± 7000
C12	572	17483	608	16446	1035	24 ± 1	2.05 ± 0.05	69000 ± 3400
C12-3	571	17513	599	16694	819	40 ± 1	3.15 ± 0.05	59000 ± 4000
mCherry-XL	558	17921	589	16978	943	70 ± 2	3.86 ± 0.05	72000 ± 4000

Table 2: Fit parameters for fluorescence lifetime measurements (decay traces and fits in SI Section 5c) along with amino acids at the four positions comprising the sequence variation (full sequences in SI Section 3).

Variant	τ_1 (ns)	a_1 (%)	τ_2 (ns)	a_2 (%)	τ_3 (ns)	a_3 (%)	τ_{av} (ns)	143	161	163	197
mCherry	1.7	83	1.0	17	-	-	1.6	W	I	Q	I
C12	2.6	64	1.1	29	0.3	7	2.0	W	I	Q	R
C12-3	3.4	93	1.1	7	-	-	3.2	I	C	L	R
mCherry-XL	3.9	97	1.1	3	-	-	3.9	S	V	Y	R

The fluorescence quantum yields of these FPs show a clear correlation with the average fluorescence lifetime (SI Figure S12a), though the trend is not perfectly linear. [5, 8] The two-fold decrease in the half-life of photobleaching with a 2.5-fold increase in fluorescence lifetime also follow expected trends, agreeing with observations of higher photobleaching for FPs with longer fluorescence lifetimes (SI Figure S6 & S7). [5, 8] Additionally, a linear fit (R_{adj}^2=0.95) of the lifetime and quantum yield resulted in a slope of 150 ± 14 μs^{-1}. Based on the relation,

$$\phi = k_r * \tau \qquad (1)$$

this slope corresponds to the rate constant of radiative decay or k_r. One can also calculate the individual rate constants for k_r and non-radiative rate (k_{nr}) for these FPs using equation 2. These values are presented in Table 3.

$$\phi = \frac{k_r}{(k_r + k_{nr})} \qquad (2)$$

Although the 1.3-fold variation in the values of k_r seems minor, the values lie outside the range predicted by the linear fit (Supplementary Figure S12b). The value of k_r can be explained by the Strickler-Berg equation, which relates radiative rate to the peak extinction coefficient and peak fluorescence frequency. [8, 30] The small variation in k_r is further corroborated by the observation that the peak extinction coefficient for this series only varies 15% from an average value of $\varepsilon_{max\ Avg}$ ~70000 $M^{-1}cm^{-1}$. This variation is modest

compared to a 1.5-fold increase of ε_{max} observed for FusionRed variants reported in our previous study. [5] However, the variation in k_r can also be attributed to the use of an average lifetime value to represent the multi-exponential fluorescence decay kinetics. The multiple timescales may reflect the presence of multiple chromophore conformations with differing absorption cross-sections. This is bolstered further by the poor linear fit between the cubed value of the emission frequency and the estimated k_r. This frequency dependence of the radiative rate, predicted by the Strickler-Berg equation, is expected to yield a linear relationship for chromophores with relatively narrow fluorescence spectra (Supplementary Figure S12c).[8, 30, 31] Most significantly, we found the value of k_{nr} undergoes the largest change (a 6.5-fold decrease) across this series. A consistent blue-shift in the absorption and emission peak wavelengths with higher brightness, correlated with this decrease in k_{nr} led us to investigate models that could explain this observation.

c. Lifetime evolution suppresses non-radiative mechanisms beyond the constraints of an energy-gap.

We first considered an Arrhenius-type dependence of the non-radiative rate constant with the transition energy, as one might expect from an "energy-gap law" (Supplementary Figure S13). [21, 22, 32] Accordingly, we assumed a single absorbing and emitting species, a lack of excited state photochemistry, and adherence to the mirror image rule of excitation and emission spectra. Under these assumptions, we estimate the 0-0 transition energy gap (ΔE_{00}) for each FP from the intersection point of the absorbance and the fluorescence spectra (Supplementary Figure S14). However, it is found that the change in non-radiative rate with ΔE_{00} is not a perfect fit for the expected exponential dependence. Additionally, we noted the Stokes-shift of mCherry (616 cm^{-1}) is smaller compared to FPs with the I197R substitution (800-1050 cm^{-1}). This observation encouraged us to examine models that consider the role of the excited state reorganization energy in addition to the energy gap. Englman and Jortner's treatment of non-radiative rate in terms of the electronic energy gap (ΔE), the excited state reorganization energy and vibrational frequencies provides a broader foundation for understanding nonradiative transition rates than the energy-gap law. [33, 34] Their theory assumes that the electronic transition (S_1 to S_0 relaxation) is coupled to the molecular vibrations and the environmental fluctuations of the bath. The highest-frequency vibrational mode in the excited electronic state serves as the primary path for non-radiative relaxation based on its coupling strength. The various limiting cases of the theory apply to strong and weak coupling in high and low temperature limits. [33-35] The strong coupling limit is applicable to systems with a large reorganization energy. In the weak coupling limit, where the role of the energy gap is dominant, the model considers a parameter γ that quantifies the role of the excited state reorganization.

The sum of mode-specific reorganization energies of the chromophore and bath nuclear motions is the reorganization energy (λ), which is typically assumed to be half of the experimentally-measured Stokes shift (λ_{SS}: Stokes shift).[36] However this approximation is accurate only for systems with Gaussian absorption and fluorescence spectra. FPs in this study also exhibit a visible 0-1 vibronic sideband along with the primary 0-0 transition, and therefore deviate strongly from Gaussian lineshapes (Figure 1c). Thus, we utilized a model provided by Jordanides *et. al* to estimate an upper limit for the reorganization energy from the spectra (Details in Supplementary Information Section 7). [37] The only assumption in this model is that the dielectric medium follows linear response. In this approach, the reorganization energy (λ_{SM}: Spectral Moment) is calculated from the normalized difference of the first moment between the absorption and fluorescence spectra around the transition energy. The values of λ_{SM} for mCherry and mCherry-XL are 812 cm^{-1} and 924 cm^{-1}, which are substantially larger than the corresponding values of 308 cm^{-1} and 472 cm^{-1} estimated from half the value of Stokes shift.

We employed these values of the reorganization energy in the Englman-Jortner low temperature/weak coupling case, as appropriate for FPs where the 0-0 peak dominates the absorption spectrum. [8, 33-35]

$$k = \frac{1}{\hbar}\frac{C^2\sqrt{2\pi}}{\sqrt{\hbar\omega_M \Delta E}}\exp -(\frac{\gamma \Delta E}{\hbar\omega_M}) \qquad (3)$$

Where k is the rate constant of non-radiative relaxation, ω_M is the frequency of the normal mode vibration of the highest frequency in the excited state of the chromophore, the parameter $\gamma \sim \log(\frac{\Delta E}{de_m}) - 1$; d is the degeneracy and e_m is the reorganization energy of the high frequency vibrational mode in the excited state. We then set $\Delta E = \Delta E_{00}$, $de_m = \lambda$, and $\omega_M = \omega_{\text{C-H Stretch}} = 3000\ cm^{-1}$. To estimate the value of Herzberg-Teller coupling (C^2), we assume the non-radiative relaxation in mCherry-XL is entirely accounted for by the Englman-Jortner model (Table 3; $k_{nr}^{Total} = k_{nr}^{E\text{-}J}$). These approximations lead to an estimate for the $C^2 = 1.45 \times 10^4\ cm^{-2}$ using λ_{SM} and $C^2 = 7.19 \times 10^5\ cm^{-2}$ using λ_{SS}. The minimal (~10%) variation in the peak frequency and intensity of the 0-0 and the 0-1 bands in the absorption spectra for these variants allow us to assume a constant value of C^2 for the other members of the series (Supplementary Section 7b). Doing so, we find small variations (of ~2%) for the pre-exponent and γ within a range of 2 to 3, which falls within the range predicted by Englman and Jortner for weakly-coupled S_1-S_0 transitions. [33-35] The results of this analysis are presented in Figure 2 and Table 3.

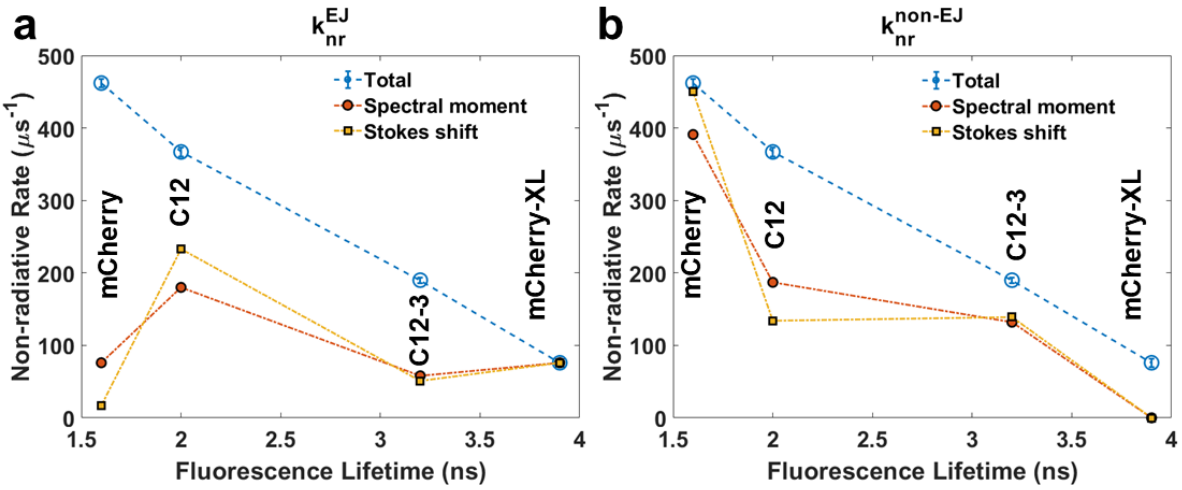

Figure 2: The non-radiative rate of the mCherry mutants obtained from the excited state lifetime and fluorescence quantum yield plotted as a function of fluorescence lifetime. (a) The non-radiative rate calculated with the low-temperature/weak-coupling limit of Englman-Jortner formalism ($k_{nr}^{E\text{-}J}$, Eqn. 3) [33-35] compared to the total non-radiative rate (k_{nr}^{Total}, Eqn. 1&2) (b) The difference between k_{nr}^{Total} and $k_{nr}^{E\text{-}J}$ of the variants, denotated as $k_{nr}^{non\ E\text{-}J}$ shown in comparison to the k_{nr}^{Total}. The data in blue circles (with standard deviations) indicate the experimental values of the k_{nr}^{Total}, whereas the data in gold and red indicate predicted values from the Englman-Jortner relationship using the reorganization energies from the Stokes shift (λ_{SS}) and the spectral moment methods (λ_{SM}) respectively. [37]

Table 3: Calculated rate constants of excited-state population decay.

Variant	ΔE_{00} (cm^{-1})	λ_{SS} (cm^{-1})	λ_{SM} (cm^{-1})	k_r (μs^{-1})	k_{nr}^{Total} (μs^{-1})	k_{nr}^{E-J} (μs^{-1})		$k_{nr}^{non\ E-J}$ (μs^{-1})	
						Spectral moment	Stokes shift	Spectral moment	Stokes shift
mCherry	16728	308	812	132 ± 5	467 ± 6	76	17	391	450
C12	16965	518	987	116 ± 6	367 ± 6	180	233	187	134
C12-3	17104	409	878	127 ± 4	190 ± 4	58	51	132	139
mCherry-XL	17450	472	924	179 ± 6	76 ± 6	76	76	0	0

Due to the small variation in the pre-exponential factor, the exponential dependence of the k_{nr} on the values of ΔE_{00} and γ dominate the value of the non-radiative rate in this model. [33, 34] We observe that k_{nr}^{E-J} differs significantly from the total non-radiative rate (k_{nr}^{Total}) for mCherry, C12, and C12-3. As a counter example, if the k_{nr}^{Total} in mCherry was a consequence of the energy gap and the reorganization energy ($k_{nr}^{Total} = k_{nr}^{E-J}$), this model would have significantly overestimated the k_{nr} for the brighter variants of this family. Thus, the net positive difference between these two values ($k_{nr}^{Total} - k_{nr}^{E-J} = k_{nr}^{non\ E-J}$), suggests mechanisms outside the scope of non-radiative relaxation from reorganization and the energy gap might be operational in mCherry and its variants, and this particular trajectory of lifetime evolution successfully suppresses this mechanism.

Discussion

We demonstrated that directed evolution of fluorescence lifetime in mCherry results in a bright fluorescent protein with a high quantum yield. The new "mCherry-XL" RFP is ~1.5-fold brighter than mCherry in mammalian cells, and its lifetime and quantum yield are on par with those of mScarlet, which is the brightest RFP to date. [6] The four mutations identified in this study are located close to the phenol end of the chromophore (Figure 3). The rotation of the phenol ring about the methine carbon (P-Bond rotation) is considered to be important for non-radiative decay. [13, 14] The spatial proximity of these mutations to the phenol moiety of the chromophore in mCherry-XL possibly impacts these motions. For example, substitution I197R was also seen in mScarlet, and the positively charged side chain is an electron withdrawing moiety capable of forming multiple hydrogen bonded contacts at this end of the chromophore. [6] The crystal structure of mScarlet (PDB: 5LK4) shows multiple hydrogen-bonded contacts for the residue R197 which results in a small dihedral angle for the P-bond in comparison to mCherry (2° vs 13°, respectively). Interestingly, all variants of mCherry after incorporating the I197R mutation displayed a higher reorganization energy in comparison to mCherry. The C12 variant (mCherry I197R) also exhibited a tri-exponential fluorescence lifetime decay. The charged nature of the sidechain at position 197 and the possibility of forming multiple hydrogen bonds may result in multiple non-interconverting chromophore conformations as reported for FPs such as TagRFP-675. [12] Additionally, the substitution Q163Y might have a similar role to play in the context of the phenol end of the chromophore. Q163 is a polar residue and the crystal structure of mCherry indicates a weak hydrogen-bond of the amine group of this sidechain (3.3 Å) with the phenolic oxygen on the chromophore (Figure 3b). Substitutions such as replacement of Q163 with an electron withdrawing and positively charged K residue have been shown to increase lifetime and quantum yield in DsRed. [22, 28] In a recent report, the substitution W143S was independently and computationally recognized in an effort to develop bright and red-shifted variants of mCherry, which

yielded the bright red-shifted RFP, mSandy2 (λ_{em} = 606 nm; ϕ =0.35).[24] The crystal structure of mCherry reveals an interaction of the indole ring on W143 with the amine group on the Q163 residue (3.4 Å).

The minor but significant variation of the extinction coefficients in these variants is correlated with the small variation of the radiative rates relative to the average value of radiative rate obtained from a linear fit of the quantum yield vs. lifetime (Supplementary Figure S12). This variation and the observed multi-exponential fits for fluorescence lifetime decays suggests the possibility of multiple emitting chromophore conformations. Structural dynamics slower than the excited state lifetime may lead to conformational diversity of environments that perturb the electronic structure of the chromophore and its radiative rate.

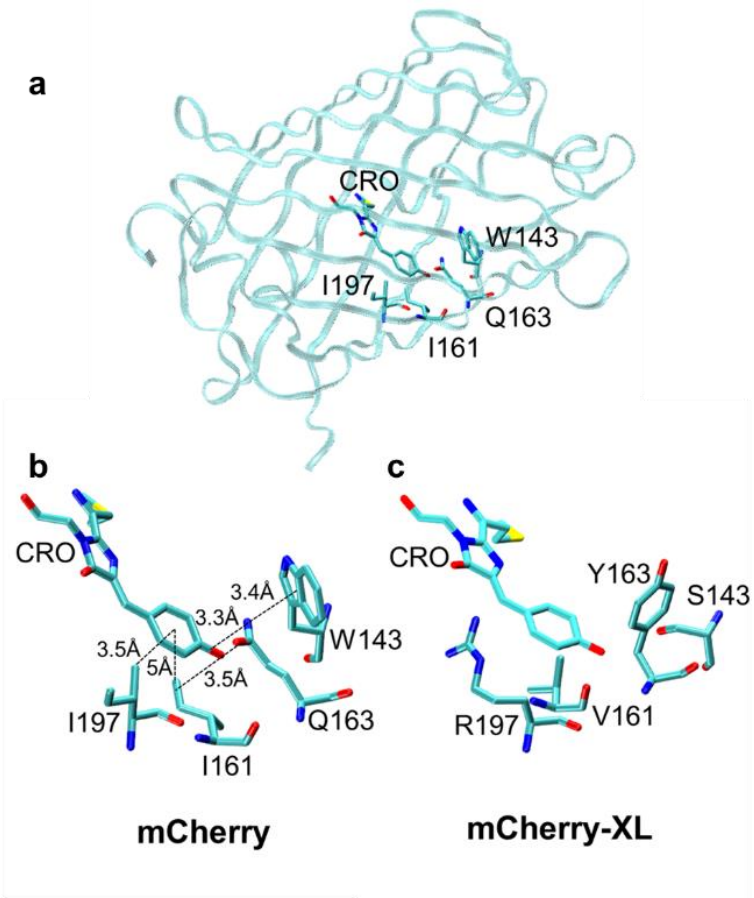

Figure 3: Insights from the crystal structure of mCherry (a) The structure of mCherry (PDB ID: 2H5Q). A detailed view of the chromophore (CRO) and the four positions identified in this study for (b) mCherry and (c) and in-silico generated structure of mCherry-XL. The dashed lines indicate the distances measured from the mCherry crystal structure. The in-silico structure was generated using the mutator plugin of the VMD molecular modelling software.[38]

The 3.2-fold increase in quantum yield across this evolution route is dominated by the reduction of the non-radiative rate which exhibits a 6.5-fold decrease across the series. The non-radiative rates of the variants are correlated with the blue-shifts of their absorption peaks. A similar correlation of blue shift with increased lifetime was observed by Canty *et. al,* who were motivated to develop a bright red-shifted FP by gene-shuffling the sequences of the far-red emitting mCardinal with the bright red mScarlet. [21] They performed selections on the resulting library based on the brightness of bacterial cultures in the 620 to 750

nm emission window. The selected variants displayed a near-linear correlation of the emission wavelength with the fluorescence lifetime. They proposed an upper limit of 625 nm for the peak emission maximum of variants created by this method. Furthermore, they concluded that far-red emitting variants are susceptible to a larger variation in spectral profiles than brighter, blue-shifted variants. Although these spectral correlations are intriguing, they did not quantify or investigate the mechanism of non-radiative decay.

The Englman-Jortner model has recently been invoked in discussions of fluorophore design. For example, modifications to this model were used to explain the low brightness of shortwave infrared fluorophores. [35] Their low quantum yields are partially explained by the high non-radiative rates resulting from high-frequency vibrations coupled to small electronic energy gaps. In contrast, when Drobizhev and co-workers plotted the values of the non-radiative rate on the logarithmic scale against the fluorescence emission frequency for a few RFPs (namely mCherry, XRFP, mPlum, DsRed2, eqFP670, and mScarlet), they found a poor agreement with the linear fit expected by Englman and Jortner's model (Supplementary Figure S13b).[14] This disagreement prompted them to consider population loss through a conical intersection seam from a twisted intermolecular charge transfer (TICT) state. Furthermore, they analyzed the strength and direction of the local electric field from the imidazolinone to the p-hydroxyphenyl ring using classical two-photon excitation spectroscopy and recognized that the local electric field around the FP chromophore controls access to the TICT states and hence can lead to ultrafast relaxation. Their analysis revealed a smaller electric field from the imidazolinone to the phenol ring potentially leads to a higher quantum yield. This can be achieved by reducing electron density at the phenolic hydroxy group through hydrogen bonds and electron-withdrawing contacts or by providing a larger electron density at the imidazolinone. These design principles corroborate findings from a hybrid QM-MM study that revealed similar ultrafast pathways for non-radiative decay in the GFP chromophore. [13] They also agree with the findings of Lin *et. al*, where stabilization of the negative charge on the phenolic oxygen atom is achieved through hydrogen-bonds between T203 and the phenolic oxygen, and/or through R96 on the imidazolinone oxygen for the GFP chromophore. Substitutions at these positions result in spectral shifts and changes in brightness. [15] These observations agree with our results where substitution of a positively charged arginine residue at the phenolic end of the chromophore in C12 variants suppressed non-radiative pathways, resulted in blue-shifts and an increased Stokes shift. Incorporation of other amino acid residues with hydrogen-bond forming side chains, e.g., serine and tyrosine in mCherry-XL resulted in further decrease in the non-radiative rate. Our efforts possibly led to the suppression of relaxation pathways that contribute to the value of $k_{nr}^{non\ E\text{-}J}$. While studies by Drobizhev *et. al*. and others provide foundations of these mechanisms for non-radiative pathways in FPs, [14, 15] they did not address the impact of lifetime based directed evolution on the pathways of excited state depopulation.

In this study, we employed the Englman-Jortner theory to model the variation in non-radiative rate for a closely-related RFP series selected through lifetime based directed evolution. [33-35] We examined whether the reduction in non-radiative rate can directly be related to the energy gap and the excited state reorganization energy. We approximated the 0-0 transition energy gap using the intersection point of the absorption and the emission spectra, and the upper-limit of excited state reorganization energy using a model provided by Jordanides *et. al*. [37] Furthermore, assuming the entire component of the observed non-radiative rate in mCherry-XL was from this formalism, we estimate a $k_{nr}^{E\text{-}J}$ value for the other members of this series. The intriguing outcome of this analysis revealed almost a 6-fold lower $k_{nr}^{E\text{-}J}$ than calculated k_{nr}^{Total} for mCherry. Though less pronounced, this observation held true for C12 and C12-3, where this model could only estimate half or less for the values of the calculated non-radiative rate. One also arrives at similar qualitative outcomes using the traditional method to estimate reorganization energy using the Stokes

shift and repeating this analysis. In such a case the $k_{nr}^{E\text{-}J}$ is >20-fold lower than the k_{nr}^{Total} for mCherry. This analysis reveals a large component of non-radiative relaxation is outside the realm of the energy-gap and is suppressed using lifetime selections. This result is consistent with the ultrafast non-radiative decay mechanisms predicted by Drobizhev *et. al* and Park *et. al.* [13, 14]

The development of highly emissive fluorophores frequently involves engineering the environment around the chromophore to make it more rigid or more viscous. [39] An issue that arises in connection with this topic is how to probe or quantify molecular rigidity with spectroscopy (i.e. with parameters beyond the ultimately desired high brightness or emission yield). One approach which has been suggested is to regard the Stokes shift, as a measure of flexibility. In principle, the Stokes shift can be calculated from the first moment of the spectral density of modes, $\rho(\omega)$ coupled to the optical transition. This $\rho(\omega)$ function, which can be quantified with time-resolved electronic spectroscopies such as photon echo techniques, represents the vibrational density of states of the system weighted by the coupling to the electronic transition. To the extent that frequency changes in the vibrational density of states reflect changes in flexibility, e.g. a shift towards high frequencies corresponds to higher rigidity, this change will be reflected in the Stokes shift. This approach to quantifying rigidity of a ligand-binding site was demonstrated using three-pulse photon echo peak shift measurements on antibody-antigen complexes, where decreases in flexibility were correlated with higher affinity binding due to specific protein-ligand interactions. [40]

In this view, a decreased Stokes shift can be interpreted to reflect a reduced flexibility of the environment, if the mutations do not strongly perturb the chromophore electronic structure. [41] This idea is central to the weak-coupling case of the Englman-Jortner theory which predicts a decreased non-radiative rate with the decrease in reorganization energy. [8, 33, 34] Unfortunately this straightforward picture of rigidifying the protein environment around the chromophore may be complicated by the strong interactions of the environment that perturb the chromophore electronic structure. For example, the mutation I197R in mCherry increases the Stokes shift despite a decrease in non-radiative rate. In contrast, an evaluation of the electro-optical properties of the GFP chromophore revealed that blue-shifted absorbers have larger Stokes-shift values. This is in-part due to a larger driving force between the two resonance forms of the chromophore. [15] Another striking counter-example is provided by AsRed2, which has only a ~5% fluorescence quantum yield, despite having a very small Stokes shift (~470 cm^{-1}) and absorption and emission peak wavelengths similar to those of several bright RFPs (λ_{abs}= 572 nm and λ_{em}=592 nm). [42] Although the low apparent brightness of this FP might be attributed to an inaccurate measurement of quantum yield owing to the kindling qualities of its parent asFP595, closer examination of other FPs with small quantum yield and modest Stokes-shifts is warranted.

It is also interesting that other examples of fluorescence lifetime evolution do not show the same spectral trends observed for mCherry-XL. For example, consider the evolution trajectory in the development of FusionRed-MQV (FR-MQV). First, a small but significant (70 cm^{-1}) decrease in Stokes shift resulted from the M42Q mutation in FusionRed. [5] Subsequently, the FR-Q, FR-MQ and FR-MQV variants had similar values of the Stokes shift (~570 cm^{-1}) although consistent decreases in the non-radiative rate (ultimately resulting in a 60% overall decrease) were observed with increased lifetime. Another example is provided by mScarlet and mScarlet-I, which have nearly identical 0-0 transition energies and nearly the same Stokes shift, yet the latter has a two-fold higher non-radiative rate. [6] Consequently, strategies beyond rigidifying the chromophore are necessary for the design of brighter FPs. [24]

These considerations suggest that large variations in absorption and emission wavelengths are possible for anionic RFP chromophores with similar values of lifetime and quantum yield, because the non-radiative rate does not depend exclusively on the transition energy gap. The RFP mScarlet is red-shifted by 10 nm (or 315 cm^{-1}) in maximum absorption and by 6 nm (or 272 cm^{-1}) in maximum emission compared to

mCherry-XL, yet it matches its quantum yield and fluorescence lifetime values. [6] The two FPs also exhibit nearly identical single exponential fluorescence lifetime decays measured using TCSPC. While the 0-0 transition energy is red-shifted by 200 cm^{-1}, the Stokes shift for mScarlet is 280 cm^{-1} smaller than that of mCherry-XL. This suggests the possibility of either red shifting mCherry-XL by reducing the Stokes-shift (while maintaining its quantum yield) or increasing the quantum yield of mScarlet by reducing its red shift. These properties are observed in AusFP1, which has a 2.7-fold smaller Stokes shift and a 1.6-fold higher quantum yield in comparison to EGFP, with the same tripeptide responsible for chromophore formation. [43] Such observations suggest the possibility of designing FPs with higher brightness without compromising on the red-shifted absorption and emission as theoretically predicted by the work of Moron *et al.* [11]

Conclusions

The race to develop bright and red-shifted fluorophores continues to drive FP engineering to newer technologies and selection schemes. Lifetime based evolution is now an established approach for delivering bright FPs such as mScarlet, mTurquoise2 and FusionRed-MQV. In this study, lifetime evolution provides a bright FP in the form of mCherry-XL and reveals the consequent co-evolution of spectral shifts, increased quantum yield, subtle changes in the radiative rate constants and very different mechanisms of suppressing non-radiative pathways. Our results strongly support recent advances by the community to understand the pathways of non-radiative depopulation of FP chromophores that lie outside the description of the energy gap. Moreover mCherry, C12, C12-3 and mCherry-XL have average fluorescence lifetimes of 1.6, 2.0, 3.2 and 3.9 ns respectively with minimal green-absorbing or emitting species, (Supplementary Figure S8) which makes them suitable for multi-color FLIM based imaging. Additionally, we do see promise in using mCherry-XL as a template for future engineering and a probe for imaging. Four amino acid substitutions on the mCherry sequence can offer solutions in the form of mCherry-XL for constructs and applications that are limited by the brightness of mCherry. Moreover, a blue-shifted absorption (~28 nm) for mCherry-XL might improve performance relative to mCherry for many FRET related applications where poor spectral overlap is observed between a green donor and a red acceptor pair. This study also shows the strength of microfluidics-based lifetime selections to enrich populations with longer lifetimes, as illustrated by the discovery of the SLT-11 variant in the EP-C12-X library. To summarize, the end-product of our selections drove us to a blue shifted variant mCherry-XL with a specific evolution trajectory based on lifetime. In a broad fitness landscape of mutations, our analysis reveals that there can be other evolution trajectories (such as the discarded clones with poor brightness or maturation) with similar end products in terms of lifetime but with different absorption and emission profiles.

SUPPORTING MATERIAL

Supplementary Information (Sections 1 to 7) has been provided to support certain results and describe techniques used in the manuscript.

Corresponding Authors:

Premashis Manna: pmanna@mit.edu

Ralph Jimenez: rjimenez@jila.colorado.edu

Author Contributions

S.M. and P.M. have equally contributed to this work. P.M, S.T.H., S.M., A.E.P. and R.J. conceptualized the study. P.M., S.M, S.T.H. F.V. and, P.F designed and performed the experiments. S.M., P.M, and S.T.H developed data analysis methods in the study. S.M., P.M., and R.J. wrote the manuscript.

Notes

The authors declare no competing financial interest.

Acknowledgements

S.M. was supported by the NIH/CU Molecular Biophysics Training Program (T32). This work was partially supported by the NSF Physics Frontier Center at JILA (PHY 1734006 to R.J.) and NIH DP1 (GM114863 to A.E.P.). S.T.H. is an ISAC Innovator. R.J. is a staff member in the Quantum Physics Division of the National Institute of Standards and Technology (NIST). Certain commercial equipment, instruments, or materials are identified in this paper in order to specify the experimental procedure adequately. Such identification is not intended to imply recommendation or endorsement by the NIST, nor is it intended to imply that the materials or equipment identified are necessarily the best available for the purpose. We acknowledge the Flow Cytometry facility at BioFrontiers Institute, CU Boulder (Grant S10ODO21601) and the BioFrontiers Institute Advanced Light Microscopy Core facility. Spectroscopy was performed at the W.M. Keck Optical Measurements Laboratory in JILA. We also thank Dr. Nancy Douglas, Connor Thomas, Dr. Jennifer Lubbeck, Dr. Brett Fiedler and Dr. Kevin Dean for valuable professional inputs at multiple stages of this work.

References

1. Dean, K. M.; Davis, L. M.; Lubbeck, J. L.; Manna, P.; Friis, P.; Palmer, A. E.; Jimenez, R. High-Speed Multiparameter Photophysical Analyses of Fluorophore Libraries. *Anal. Chem.* **2015**, *87* (10), 5026–5030. https://doi.org/10.1021/acs.analchem.5b00607

2. Hung, S. T.; Mukherjee, S.; Jimenez, R. Enrichment of Rare Events Using a Multi-Parameter High Throughput Microfluidic Droplet Sorter. *Lab Chip* **2020**, *20* (4), 834–843. https://doi.org/10.1039/c9lc00790c.

3. Bindels, D. S.; Postma, M.; Haarbosch, L.; van Weeren, L.; Gadella, T. W. J. Multiparameter Screening Method for Developing Optimized Red-Fluorescent Proteins. *Nat. Protoc.* **2020**, *15* (2), 450–478. https://doi.org/10.1038/s41596-019-0250-7.

4. Manna, P.; Hung, S. T.; Mukherjee, S.; Friis, P.; Simpson, D. M.; Lo, M. N.; Palmer, A. E.; Jimenez, R. Directed Evolution of Excited State Lifetime and Brightness in FusionRed Using a Microfluidic Sorter. *Integr. Biol. (United Kingdom)* **2018**, *10* (9), 516–526. https://doi.org/10.1039/c8ib00103k.

5. Mukherjee, S.; Hung, S. T.; Douglas, N.; Manna, P.; Thomas, C.; Ekrem, A.; Palmer, A. E.; Jimenez, R. Engineering of a Brighter Variant of the Fusionred Fluorescent Protein Using Lifetime Flow Cytometry and Structure-Guided Mutations. *Biochemistry* **2020**, *59* (39), 3669–3682. https://doi.org/10.1021/acs.biochem.0c00484.

6. Bindels, D. S.; Haarbosch, L.; Van Weeren, L.; Postma, M.; Wiese, K. E.; Mastop, M.; Aumonier, S.; Gotthard, G.; Royant, A.; Hink, M. A.; Gadella, T. W. J. MScarlet: A Bright Monomeric Red Fluorescent Protein for Cellular Imaging. *Nat. Methods* **2016**, *14* (1), 53–56. https://doi.org/10.1038/nmeth.4074.

7. Goedhart, J.; Von Stetten, D.; Noirclerc-Savoye, M.; Lelimousin, M.; Joosen, L.; Hink, M. A.; Van Weeren, L.; Gadella, T. W. J.; Royant, A. Structure-Guided Evolution of Cyan Fluorescent Proteins towards a Quantum Yield of 93%. *Nat. Commun.* **2012**, *3*. https://doi.org/10.1038/ncomms1738.

8. Mukherjee, S.; Jimenez, R. Photophysical Engineering of Fluorescent Proteins: Accomplishments and Challenges of Physical Chemistry Strategies. *J. Phys. Chem. B* **2022**, *126* (4), 735–750. https://doi.org/10.1021/acs.jpcb.1c05629.

9. Miyawaki, A.; Shcherbakova, D. M.; Verkhusha, V. V. Red Fluorescent Proteins: Chromophore Formation and Cellular Applications. *Curr. Opin. Struct. Biol.* **2012**, *22* (5), 679–688. https://doi.org/10.1016/j.sbi.2012.09.002.

10. Bravaya, K. B.; Subach, O. M.; Korovina, N.; Verkhusha, V. V.; Krylov, A. I. Insight into the Common Mechanism of the Chromophore Formation in the Red Fluorescent Proteins: The Elusive Blue Intermediate Revealed. J. Am. Chem. Soc. 2012, 134 (5), 2807–2814. https://doi.org/10.1021/ja2114568.

11. Moron, V.; Marazzi, M.; Wanko, M. Far Red Fluorescent Proteins: Where Is the Limit of the Acylimine Chromophore? *J. Chem. Theory Comput.* **2019**, *15* (7), 4228–4240. https://doi.org/10.1021/acs.jctc.9b00070.

12. Konold, P. E.; Yoon, E.; Lee, J.; Allen, S. L.; Chapagain, P. P.; Gerstman, B. S.; Regmi, C. K.; Piatkevich, K. D.; Verkhusha, V. V.; Joo, T.; Jimenez, R. Fluorescence from Multiple Chromophore Hydrogen-Bonding States in the Far-Red Protein TagRFP675. *J. Phys. Chem. Lett.* **2016**, *7* (15), 3046–3051. https://doi.org/10.1021/acs.jpclett.6b01172.

13. Park, J. W.; Rhee, Y. M. Electric Field Keeps Chromophore Planar and Produces High Yield Fluorescence in Green Fluorescent Protein. *J. Am. Chem. Soc.* **2016**, *138* (41), 13619–13629. https://doi.org/10.1021/jacs.6b06833.

14. Drobizhev, M.; Molina, R. S.; Callis, P. R.; Scott, J. N.; Lambert, G. G.; Salih, A.; Shaner, N. C.; Hughes, T. E. Local Electric Field Controls Fluorescence Quantum Yield of Red and Far-Red Fluorescent Proteins. *Front. Mol. Biosci.* **2021**, *8* (February), 1–21. https://doi.org/10.3389/fmolb.2021.633217.

15. Lin, C. Y.; Romei, M. G.; Oltrogge, L. M.; Mathews, I. I.; Boxer, S. G. Unified Model for Photophysical and Electro-Optical Properties of Green Fluorescent Proteins. *J. Am. Chem. Soc.* **2019**, *141* (38), 15250–15265. https://doi.org/10.1021/jacs.9b07152.

16. Romei, M. G.; Lin, C. Y.; Mathews, I. I.; Boxer, S. G. Electrostatic Control of Photoisomerization Pathways in Proteins. *Science (80-.).* **2020**, *367* (6473), 76–79. https://doi.org/10.1126/science.aax1898.

17. Lin, C.-Y.; Romei, M.; Mathews, I.; Boxer, S. Energetic Basis of Excited-State Enzyme Design and Function. *ChemRxiv* **2021**. https://doi.org/10.33774/chemrxiv-2021-9l2vn

18. List, N. H.; Jones, C. M.; Martínez, T. J. Internal Conversion of the Anionic GFP Chromophore: In and out of the I-Twisted S1/S0conical Intersection Seam. *Chem. Sci.* **2022**, *13* (2), 373–385. https://doi.org/10.1039/d1sc05849e.

19. Romero, P. A.; Arnold, F. H. Exploring Protein Fitness Landscapes by Directed Evolution. *Nat. Rev. Mol. Cell Biol.* **2009**, *10* (12), 866–876. https://doi.org/10.1038/nrm2805.

20. Specht, E. A.; Braselmann, E.; Palmer, A. E. A Critical and Comparative Review of Fluorescent Tools for Live-Cell Imaging. *Annu. Rev. Physiol.* **2017**, *79* (1), 93–117. https://doi.org/10.1146/annurev-physiol-022516-034055.

21. Canty, L.; Hariharan, S.; Liu, Q.; Haney, S. A.; Andrews, D. W. Peak Emission Wavelength and Fluorescence Lifetime Are Coupled in Far-Red, GFP-like Fluorescent Proteins. *PLoS One* **2018**, *13* (11), e0208075.

22. Shu, X.; Shaner, N. C.; Yarbrough, C. A.; Tsien, R. Y.; Remington, S. J. Novel Chromophores and Buried Charges Control Color in MFruits. *Biochemistry* **2006**, *45* (32), 9639–9647. https://doi.org/10.1021/bi060773l.

23. Acharya, A.; Bogdanov, A. M.; Grigorenko, B. L.; Bravaya, K. B.; Nemukhin, A. V.; Lukyanov, K. A.; Krylov, A. I. Photoinduced Chemistry in Fluorescent Proteins: Curse or Blessing? *Chemical Reviews*. 2017, pp 758–795. https://doi.org/10.1021/acs.chemrev.6b00238.

24. Legault, S.; Fraser-Halberg, D. P.; McAnelly, R. L.; Eason, M. G.; Thompson, M. C.; Chica, R. A. Generation of Bright Monomeric Red Fluorescent Proteins via Computational Design of Enhanced Chromophore Packing. *Chem. Sci.* **2022**. https://doi.org/10.1039/d1sc05088e.

25. Onukwufor, J. O.; Trewin, A. J.; Baran, T. M.; Almast, A.; Foster, T. H.; Wojtovich, A. P. Quantification of Reactive Oxygen Species Production by the Red Fluorescent Proteins KillerRed, SuperNova and mCherry. *Free Radic. Biol. Med.* **2020**, *147*, 1–7. https://doi.org/https://doi.org/10.1016/j.freeradbiomed.2019.12.008.

26. Scaramuzzino, C.; Cuoc, E. C.; Pla, P.; Humbert, S.; Saudou, F. Calcineurin and Huntingtin Form a Calcium-Sensing Machinery That Directs Neurotrophic Signals to the Nucleus. *Sci. Adv.* **2022**, *8* (1), eabj8812. https://doi.org/10.1126/sciadv.abj8812.

27. Shaner, N. C.; Campbell, R. E.; Steinbach, P. A.; Giepmans, B. N. G.; Palmer, A. E.; Tsien, R. Y. Improved Monomeric Red, Orange and Yellow Fluorescent Proteins Derived from Discosoma Sp. Red Fluorescent Protein. *Nat. Biotechnol.* **2004**, *22* (12), 1567–1572. https://doi.org/10.1038/nbt1037.

28. Chica, R. A.; Moore, M. M.; Allen, B. D.; Mayo, S. L. Generation of Longer Emission Wavelength Red Fluorescent Proteins Using Computationally Designed Libraries. *Proc. Natl. Acad. Sci. U. S. A.* **2010**, *107* (47), 20257–20262. https://doi.org/10.1073/pnas.1013910107.

29. Shen, Y.; Chen, Y.; Wu, J.; Shaner, N. C.; Campbell, R. E. Engineering of mCherry Variants with Long Stokes Shift, Red-Shifted Fluorescence, and Low Cytotoxicity. *PLoS One* **2017**, *12* (2). https://doi.org/10.1371/journal.pone.0171257.

30. Strickler, S. J.; Berg, R. A. Relationship between Absorption Intensity and Fluorescence Lifetime of Molecules. J. Chem. Phys. 1962, 37 (4), 814–822. https://doi.org/10.1063/1.1733166.

31. Jung, G.; Brockhinke, A.; Gensch, T.; Hötzer, B.; Schwedler, S.; Veettil, S. K. Fluorescence Lifetime of Fluorescent Proteins. In Fluorescent Proteins I: From Understanding to Design; Jung, G., Ed.; Springer Berlin Heidelberg: Berlin, Heidelberg, 2011; pp 69–97. https://doi.org/10.1007/4243_2011_14.

32. Mauring, K.; Krasnenko, V.; Miller, S. Photophysics of the Blue Fluorescent Protein. *J. Lumin.* **2007**, *122–123* (1–2), 291–293. https://doi.org/10.1016/j.jlumin.2006.01.144.

33. Englman, R.; Jortner, J. The Energy Gap Law for Radiationless Transitions in Large Molecules. *Mol. Phys.* **1970**, *18* (2), 285–287. https://doi.org/10.1080/00268977000100171.

34. Jang, S. J. A Simple Generalization of the Energy Gap Law for Nonradiative Processes. J. Chem. Phys. 2021, 155 (16), 164106. https://doi.org/10.1063/5.0068868.

35. Friedman, H. C.; Cosco, E. D.; Atallah, T. L.; Jia, S.; Sletten, E. M.; Caram, J. R. Establishing Design Principles for Emissive Organic SWIR Chromophores from Energy Gap Laws. *Chem* **2021**, *7* (12), 3359–3376. https://doi.org/10.1016/j.chempr.2021.09.001.

36. Mertz, E. L.; Tikhomirov, V. A.; Krishtalik, L. I. Stokes Shift as a Tool for Probing the Solvent Reorganization Energy. *J. Phys. Chem. A* **1997**, *101* (19), 3433–3442. https://doi.org/10.1021/jp963042b.

37. Jordanides, X. J.; Lang, M. J.; Song, X.; Fleming, G. R. Solvation Dynamics in Protein Environments Studied by Photon Echo Spectroscopy. *J. Phys. Chem. B* **1999**, *103* (37), 7995–8005. https://doi.org/10.1021/jp9910993.

38. Humphrey, W.; Dalke, A.; Schulten, K. VMD: Visual Molecular Dynamics. *J. Mol. Graph.* **1996**, *14* (1), 33–38. https://doi.org/10.1016/0263-7855(96)00018-5.

39. Lavis, L. D.; Raines, R. T. Bright Ideas for Chemical Biology. *ACS Chem. Biol.* **2008**, *3* (3), 142–155. https://doi.org/10.1021/cb700248m.

40. Jimenez, R.; Salazart, G.; Baldridge, K. K.; Romesberg, F. E. Flexibility and Molecular Recognition in the Immune System. *Proc. Natl. Acad. Sci. U. S. A.* **2003**, *100* (1), 92–97. https://doi.org/10.1073/pnas.262411399.

41. Shaner, N. C.; Patterson, G. H.; Davidson, M. W. Advances in Fluorescent Protein Technology. *J. Cell Sci.* **2007**, *120* (24), 4247–4260. https://doi.org/10.1242/jcs.005801.

42. Shkrob, M. A.; Yanushevich, Y. G.; Chudakov, D. M.; Gurskaya, N. G.; Labas, Y. A.; Poponov, S. Y.; Mudrik, N. N.; Lukyanov, S.; Lukyanov, K. A. Far-Red Fluorescent Proteins Evolved from a Blue Chromoprotein from Actinia Equina. *Biochem. J.* **2005**, *392* (3), 649–654. https://doi.org/10.1042/BJ20051314.

43. Lambert, G. G.; Depernet, H.; Gotthard, G.; Schultz, D. T.; Navizet, I.; Lambert, T.; Adams, S. R.; Torreblanca-Zanca, A.; Chu, M.; Bindels, D. S.; Levesque, V.; Moffatt, J. N.; Salih, A.; Royant, A.; Shaner, N. C. Aequorea's Secrets Revealed: New Fluorescent Proteins with Unique Properties for Bioimaging and Biosensing. *PLoS Biol.* **2020**, *18* (11). https://doi.org/10.1371/journal.pbio.3000936.